An Improved Active Damping Method with Capacitor Current Feedback

Yi-Wen Geng*, Ya-Wen Qi*, Hai-Wei Liu*, Fei Guo*, Peng-Fei Zheng*, Yong-Gang Li*, and Wen-Ming Dong†

*,†School of Electrical and Power Engineering, China University of Mining and Technology, Xuzhou, China

Abstract

Proportional capacitor current feedback active damping (CCFAD) has a limited valid damping region in the discrete time domain as (0, f_s/6). However, the resonance frequency (f_r) of an LCL-type filter is usually designed to be less than half the sampling frequency (f_s) with the symmetry regular sampling method. Therefore, (f_s/6, f_s/2) becomes an invalid damping region. This paper proposes an improved CCFAD method to extend the valid damping region from (0, f_s/6) to (0, f_s/2), which covers all of the possible resonance frequencies in the design procedure. The full-valid damping region is obtained and the stability margin of the system is analyzed in the discrete time domain with the Nyquist criterion. Results show that the system can operate stably with the proposed CCFAD method when the resonance frequency is in the region (0, f_s/2). The performances at the steady and dynamic state are enhanced by the selected feedback coefficient H and controller gain K_p. Finally, the feasibility and effectiveness of the proposed CCFAD method are verified by simulation and experimental results.

Key words: Active damping, Capacitor current feedback, Damping region, LCL filter

I. INTRODUCTION

Photovoltaic generation, as one of the most promising approaches for developing renewable energy, has been widely used. As a key piece of equipment in PV systems, the grid-connected inverter transforms DC current into AC current and injects it into the grid. A filter between the inverter and the grid is indispensable in PV grid-connected systems for attenuating the high order output current harmonics. As for the filter, an LCL-type filter provides better performance with a reduced cost and weight when compared to the traditional L-type filter [1], [2]. However, the three-order structure of the LCL filter makes it easier to resonate. Thus, it is necessary to add a damping algorithm.

Passive damping and active damping are two major alternatives of suppressing the resonance caused by an LCL filter. Passive damping is realized by adding extra resistors in series or parallel with the capacitors or inductors of LCL filters [3]-[5]. Although passive damping is easy to be realized, the power consumption on the passive components is counterproductive to the concept of energy saving. The active damping methods, such as virtual resistor algorithms [6]-[8], adopt special control strategies to achieve the same performance. When compared to passive damping methods, the absence of loss is the most obvious advantage.

Capacitor current feedback active damping (CCFAD) is extensively used due to its simple structure and easy implementation [9]-[11]. The conventional transfer function of CCFAD is analyzed and calculated in the continuous time domain [12], [13], which is inaccurate in digital control systems. In [14], the steady state characteristic of CCFAD in the discrete time domain is discussed and the optimal design of the feedback coefficient is proposed. In [15], the proportional and integral coefficients are optimized for the proportional integral (PI) controller used in CCFAD. In [16], it is indicated that a CCFAD system in the discrete time domain has a specific valid damping region. In addition, if the actual resonance frequency is higher than 1/6 of the sampling frequency f_s, the grid-connected system becomes unstable easily. In [17], the computation time of a CCFAD system is reduced to achieve high robustness against the grid impedance variations. Although the open-loop unstable poles are removed in [17], the valid damping region is still within (0, f_s/6), which causes some difficulties for parameter design. In [18], the valid damping region is extended to (0, f_s/4).

However, the sampling frequency f_s needs to be twice the switching frequency f_{sw}, which introduces limitations on some applications. The area equivalence method is adopted in [19] to implement time delay compensation. However, its compensation time is less than $0.5T_s$. The authors of [20] used capacitor current feedback through a second-order high pass filter to extend the valid damping region. However, the filter has many parameters that are difficult to design. In [21], the time delay compensation is realized by inserting a second-order lead-lag compensator into the active damping loop based on a first-order *Padé* approximation. However, the valid damping region is only (0, f_s/3). In addition, the compensator structure is complex.

This paper proposes an improved CCFAD method that can provide a full-valid damping region, i.e., (0, f_s/2), to ensure that all of the possible frequencies are covered when designing an LCL filter. The stability margin is analyzed in the discrete time domain for selecting the proper feedback coefficient H and the controller gain K_P. Simulation and experiment results have verified the effectiveness and feasibility of the proposed method.

II. Structure and Model of the Inverter

Fig. 1 shows the structure of an LCL-type three-phase voltage source inverter. L_1, L_2 and C are the inverter-side filter inductor, the grid-side filter inductor and the filter capacitor, respectively. C_{dc} denotes the dc-side capacitor. v_{ca}, v_{cb}, v_{cc} are the filter capacitor voltage. v_{ga}, v_{gb}, v_{gc} are the grid voltage. v_{dc} and i_{dc} represent the dc-side voltage and current.

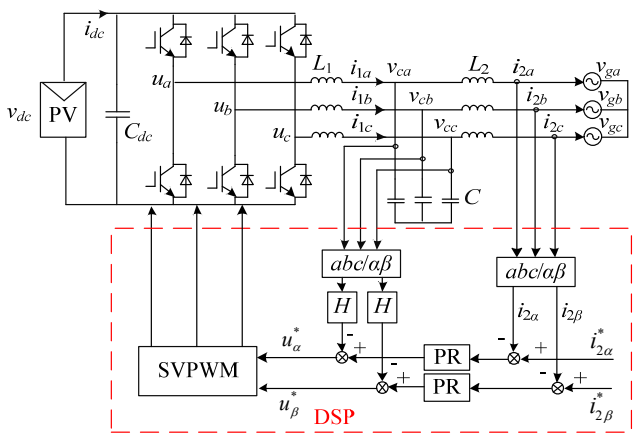

Fig. 1. System structure of an LCL-type three-phase grid-connected inverter.

Voltage space vector pulse width modulation (SVPWM) is adopted here. In the $\alpha\beta$ stationary frame, a proportional resonant (PR) controller is applied to track the current reference with zero steady state error. The grid-side current is sensed and fed back to obtain a high quality output current. Fig. 2 shows an equivalent diagram of the proportional CCFAD system in the continuous time domain. In Fig. 2, T_s is a sampling period. The equivalent gain of the inverter K_{PWM} is 1 when SVPWM is adopted. H is the proportional feedback coefficient. In addition, a sampling delay exists in the PWM modulation process, which can be described as a zero-order holder (ZOH).

The computation is implemented by a digital signal processing (DSP) chip. A computation delay is introduced because the present calculation adopts the previous beat sampling value, which can be thought of as one sampling period [22]. The transfer function of the computation delay $G_d(s)$ can be expressed as (1).

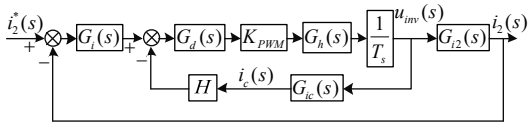

Fig. 2. Diagram of the proportional CCFAD system in the continuous time domain.

$$G_d(s) = e^{-sT_s} \tag{1}$$

The transfer function of the ZOH is:

$$G_h(s) = \frac{1 - e^{-sT_s}}{s} \tag{2}$$

A quasi-proportional resonant controller is adopted here for a wide bandwidth, and the transfer function is:

$$G_i(s) = K_p + K_r \cdot \frac{2\omega_c s}{s^2 + 2\omega_c s + \omega_1^2} \tag{3}$$

Where K_p is the proportional gain, and K_r is the integral gain [23]. ω_1 and ω_c are the fundamental frequency and cut-off angular frequency.

The transfer function $G_{i2}(s)$ from grid-side current to the inverter-side voltage is:

$$G_{i2}(s) = \frac{i_2(s)}{u_{inv}(s)} = \frac{1}{sCL_1L_2} \cdot \frac{1}{s^2 + \omega_r^2} \tag{4}$$

The transfer function $G_{ic}(s)$ from the capacitor current to the inverter-side voltage is:

$$G_{ic}(s) = \frac{i_c(s)}{u_{inv}(s)} = \frac{1}{L_1} \cdot \frac{s}{s^2 + \omega_r^2} \tag{5}$$

In (4) and (5), ω_r represents the inherent resonance angular frequency.

$$\omega_r = \sqrt{\frac{L_1 + L_2}{CL_1L_2}} \tag{6}$$

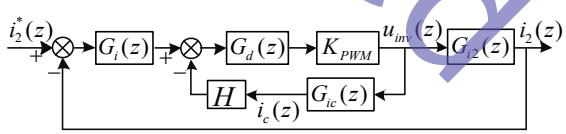

Fig. 3. Diagram of the proportional CCFAD system in the discrete time domain.

Fig. 3 shows a current control diagram of the proportional CCFAD system in the discrete time domain. $G_{ic}(s)$ and $G_{i2}(s)$ can be rewritten as $G_{ic}(z)$ and $G_{i2}(z)$, which are:

$$G_{ic}(z)=\frac{\sin(\omega_r T_s)}{\omega_r L_1}\cdot\frac{z-1}{z^2-2z\cos(\omega_r T_s)+1} \tag{7}$$

$$G_{i2}(z)=\frac{T_s}{\omega_r^2 CL_1L_2}\cdot\frac{1}{z-1}-\frac{\sin(\omega_r T_s)}{\omega_r^3 CL_1L_2}\cdot\frac{z-1}{z^2-2z\cos(\omega_r T_s)+1} \tag{8}$$

In Fig. 3, the open-loop transfer function of the proportional CCFAD system in the discrete time domain can be derived as (9).

$$T(z)=\frac{G_i(z)K_{PWM}}{\omega_r(L_1+L_2)}\cdot\frac{\omega_r T_s[z^2-2z\cos(\omega_r T_s)+1]-(z-1)^2\sin(\omega_r T_s)}{(z-1)\left[z(z^2-2z\cos(\omega_r T_s)+1)+\frac{K_{PWM}H\sin(\omega_r T_s)}{\omega_r L_1}(z-1)\right]} \tag{9}$$

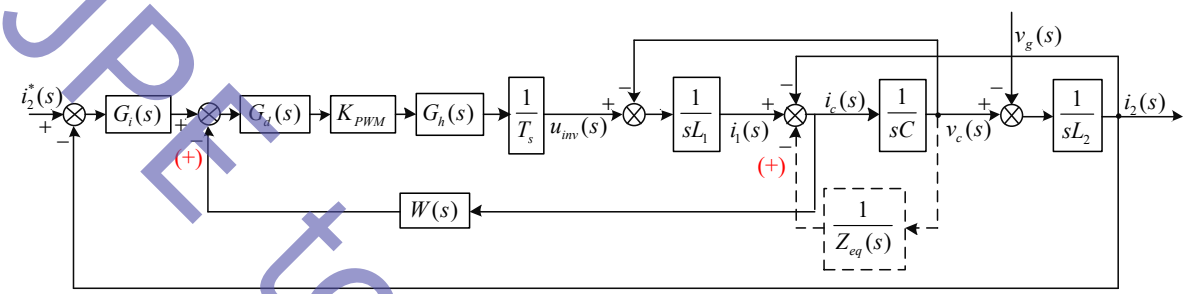

Fig. 5. Diagram of the improved CCFAD in the continuous time domain.

III. Stability Analysis of the Proposed CCFAD

The condition $f_r < f_s/2$ is required in the parameter designing procedure when the symmetry regular sampling method is adopted [24]. Here, the designing constraint (0, $f_s/2$) is defined as the resonance frequency region. If the resonance frequency is designed so that it is higher than the valid damping region (0, $f_s/6$) in the conventional CCFAD [25], the system becomes potentially unstable due to grid impedance variations. Therefore, the parameter designing is limited to (0, $f_s/6$). Meanwhile, if the valid damping region is extended to (0, $f_s/2$), which covers the entire resonance frequency region, it becomes much easier to design the LCL parameters. In this paper, the extended valid damping region (0, $f_s/2$) is defined as the full-valid damping region.

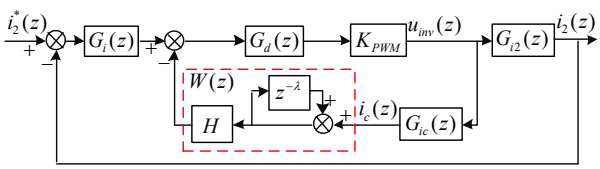

Fig. 4. Diagram of the improved CCFAD in the discrete time domain.

A diagram of the proposed CCFAD in the discrete time domain is shown in Fig. 4, and the transfer function $W(z)$ can be described as:

$$W(z)=\frac{H}{1-z^{-\lambda}} \tag{10}$$

Where λ is an adjustable parameter.

Furthermore, in the continuous time domain, (10) can be described as:

$$W(s)=\frac{H}{1-e^{-\lambda sT_s}} \tag{11}$$

A diagram of the proposed CCFAD in the continuous time domain is shown in Fig. 5. Through a series of equivalent transformations, the feedback of capacitor current can be seen as a virtual impedance $Z_{eq}(s)$ paralleled with the filter capacitor, shown as the dashed box in Fig. 5. $Z_{eq}(s)$ can be expressed as:

$$Z_{eq}(s)=\frac{L_1T_s}{CK_{PWM}}\cdot\frac{1}{W(s)}\cdot\frac{e^{sT_s}s}{1-e^{-sT_s}} \tag{12}$$

A. Selection of λ

Applying $s = j\omega$ to $W(s)$ yields $Z_{eq}(j\omega)$ as in (13). $Z_{eq}(j\omega)$ can be regarded as a resistor paralleled with a reactor, and the paralleled impedance can be expressed as:

$$Z_{eq}(j\omega)=R_{eq}(\omega)//X_{eq}(\omega) \tag{14}$$

The equivalent resistance and reactance can be expressed as:

$$R_{eq}(\omega)=\frac{-L_1}{CHK_{PWM}}\cdot\frac{\omega T_s\sin(0.5\lambda\omega T_s)}{\sin(0.5\omega T_s)\sin(1.5-0.5\lambda)\omega T_s} \tag{15}$$

$$X_{eq}(\omega)=\frac{L_1}{CHK_{PWM}}\cdot\frac{\omega T_s\sin(0.5\lambda\omega T_s)}{\sin(0.5\omega T_s)\cos(1.5-0.5\lambda)\omega T_s} \tag{16}$$

$R_{eq}(\omega)$ plays the role of damping the resonance peak. Therefore, (15) needs to be positive. In order to obtain the full-valid damping region, (17) must be satisfied.

$$\begin{cases}\sin(0.5\lambda\omega T_s)>0\\ \sin(1.5-0.5\lambda)\omega T_s>0\end{cases} \tag{17}$$

However, $\sin(0.5\omega T_s)$ is higher than zero when $\omega < \omega_s$, which causes $R_{eq}(\omega) < 0$. Therefore, the feedback in Fig. 5 is

modified as a positive feedback. Accordingly, the minus sign in Fig. 5 is replaced by the plus sign shown in the bracket.

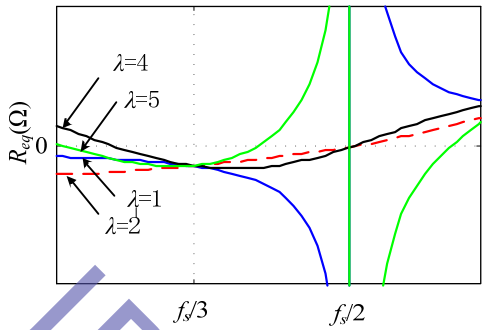

Fig. 6. Curves of the equivalent resistance when λ= 1, 2, 4, 5.

Fig. 6 shows the equivalent resistance according to (15) with different values of λ. The possible values of λ are λ = 1 and λ = 2 to satisfy (17) and to cover (0, f_s/2). Based on (9) and (10), the modified open-loop transfer function of the proposed CCFAD system can be derived as (18).

$$Z_{eq}(j\omega)=\frac{L_1}{CHK_{PWM}}\cdot\frac{j\omega T_s(1-e^{-\lambda j\omega T_s})e^{j\omega T_s}}{1-e^{-j\omega T_s}}=\frac{L_1}{CHK_{PWM}}\cdot\frac{\omega T_s}{\sin(0.5\omega T_s)}\sin(0.5\lambda\omega T_s)\cdot\left[-\sin(1.5-0.5\lambda)\omega T_s+j\cos(1.5-0.5\lambda)\omega T_s\right] \quad (13)$$

$$T_{imp}(z)=\frac{G_i(z)K_{PWM}}{\omega_r(L_1+L_2)}\frac{(z^{\lambda}-1)\left[\omega_r T_s(z^2-2z\cos(\omega_r T_s)+1)-(z-1)^2\sin(\omega_r T_s)\right]}{(z-1)\left[z(z^{\lambda}-1)(z^2-2z\cos(\omega_r T_s)+1)-\frac{K_{PWM}H\sin(\omega_r T_s)}{\omega_r L_1}(z^{\lambda+1}-z^{\lambda})\right]} \quad (18)$$

$$T_{imp}(z,2)=\frac{G_i(z)K_{PWM}}{\omega_r(L_1+L_2)}\cdot\frac{(z+1)\left[\omega_r T_s\left(z^2-2z\cos(\omega_r T_s)+1\right)-(z-1)^2\sin(\omega_r T_s)\right]}{z(z-1)\left[(z+1)\left(z^2-2z\cos(\omega_r T_s)+1\right)-\frac{K_{PWM}H\sin(\omega_r T_s)}{\omega_r L_1}z\right]} \quad (19)$$

The Nyquist stability criterion in the discrete time domain is similar to that in the continuous time domain. In order to investigate the stability of the proposed CCFAD system, the numbers of unstable open-loop poles (N) and -180° crossings need to be discussed.

B. Stability Analysis of the Proposed CCFAD with λ = 2

When λ = 2, the open-loop transfer function can be expressed as (19). There are five open-loop poles, and two of them are stable poles (P_1 = 1, P_2 = 0).

Define the denominator of (19) as (20).

$$D(z,2)=(z+1)\left[z^2-2z\cos(\omega_r T_s)+1\right]-\frac{K_{PWM}H\sin(\omega_r T_s)}{\omega_r L_1}z \quad (20)$$

The Routh-Hurwitz criterion is adopted to determine the numbers of unstable open-loop poles after a *w*-transformation, and the Routh array is as:

$$\begin{array}{ll} w^3: & A \qquad\qquad -A \\ w^2: & -\left[4+4\cos(\omega_r T_s)+A\right] \quad A-4+4\cos(\omega_r T_s) \\ w^1: & \dfrac{-8A}{A+4+4\cos(\omega_r T_s)} \\ w^0: & A-4+4\cos(\omega_r T_s) \end{array}$$

where:

$$A=\frac{K_{PWM}H\sin(\omega_r T_s)}{\omega_r L_1} \quad (21)$$

A bode diagram of the improved CCFAD system when λ = 2 is plotted as Fig. 7, and it can be discussed in the following two situations depending on H_1.

(1) 0 <H < H_1, N = 1. It can be found in Fig. 7 that the phase crosses -180° once, which makes the system unstable.

(2) H > H_1, N = 2. There is no -180° crossing. Therefore, the system is unstable, where:

$$H_1=\frac{4\omega_r L_1[1-\cos(\omega_r T_s)]}{K_{PWM}\sin(\omega_r T_s)} \quad (22)$$

According to the stability criterion in the discrete time domain, the proposed CCFAD system with λ = 2 always has unstable open-loop poles and the phase plot cannot meet the stability requirements as per the previous analysis. Therefore, λ = 2 is abandoned.

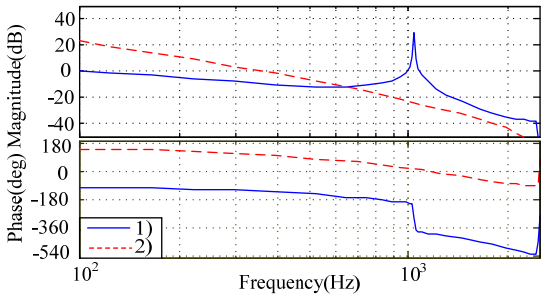

Fig. 7. Bode diagram of the improved CCFAD system when $\lambda = 2$.

C. Stability Analysis of the Proposed CCFAD with $\lambda = 1$

According to (15) and (16), the paralleled equivalent resistance $R_{eq}(\omega)$ and reactance $X_{eq}(\omega)$ vary with ω as shown in Fig. 8. It can be seen that the proposed CCFAD method makes it possible for $R_{eq}(\omega)$ to be negative in $(0, f_s/2)$. Thus, changing the negative feedback in the inner loop to positive feedback can make $R_{eq}(\omega)$ positive, as shown in Fig.5. Then the valid damping region is extended to $f_s/2$.

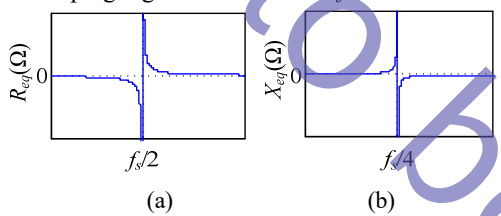

Fig. 8. Curves of the equivalent resistance and reactance with $\lambda = 1$: (a) Equivalent resistance R_{eq}; (b) Equivalent reactance X_{eq}.

According to (18), the open-loop transfer function can be expressed as (23) when $\lambda = 1$. There are four poles in (23), and two of them are stable poles ($P_1 = 1$, $P_2 = 0$).

Similarly, define the denominator in (23) as:

$$D(z,1) = z^2 - 2z\cos(\omega_r T_s) + 1 - \frac{K_{PWM} H \sin(\omega_r T_s)}{\omega_r L_1} \tag{24}$$

$$T_{imp}(z,1) = \frac{G_i(z) K_{PWM}}{\omega_r (L_1 + L_2)} \frac{\omega_r T_s [z^2 - 2z\cos(\omega_r T_s) + 1] - (z-1)^2 \sin(\omega_r T_s)}{z(z-1)\left[z^2 - 2z\cos(\omega_r T_s) + 1 - \frac{K_{PWM} H \sin(\omega_r T_s)}{\omega_r L_1}\right]} \tag{23}$$

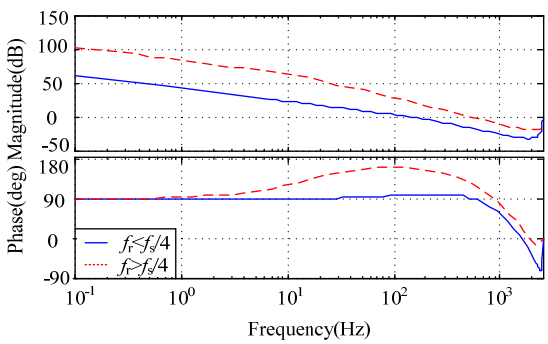

Fig. 9. Bode diagram of the third condition of the improved CCFAD system when $\lambda = 1$.

D. Effect of Paralleled Virtual Impedance on the Resonance Frequency

In the improved system, the virtual impedance algorithm changes the original resonance frequency. This part will discuss the resonance frequency shifting related to the virtual impedance.

According to the Routh-Hurwitz criterion after a w-transformation, the Routh array is shown as follows.

$$\begin{array}{ll} w^2: 2 - A + 2\cos(\omega_r T_s) & 2 - A - 2\cos(\omega_r T_s) \\ w^1: \quad 2A & 0 \\ w^0: 2 - A - 2\cos(\omega_r T_s) & \end{array}$$

Three conditions can be summarized as follows to investigate unstable open-loop poles by analyzing the first column of the Routh array.

(1) $f_r < f_s/4$ when $0 < H < H_2$ or $f_r > f_s/4$ when $0 < H < H_3$. In this case, the sign of the first column in the Routh array is positive and the numbers of unstable poles $N = 0$, where:

$$H_2 = \frac{2\omega_r L_1 [1 - \cos(\omega_r T_s)]}{K_{PWM} \sin(\omega_r T_s)},\ H_3 = \frac{2\omega_r L_1 [1 + \cos(\omega_r T_s)]}{K_{PWM} \sin(\omega_r T_s)} \tag{25}$$

(2) $f_r < f_s/4$ when $H_2 < H < H_3$ or $f_r > f_s/4$ when $H_3 < H < H_2$. In this case, the sign of the first column in the Routh array changes once and the numbers of unstable poles $N = 1$.

(3) $f_r < f_s/4$ when $H > H_3$ or $f_r > f_s/4$ when $H > H_2$. In this case, the sign of the first column in the Routh array changes twice and the numbers of unstable poles $N = 2$.

In the second case, the numbers of unstable poles $N = 1$, and the system is unstable. As for the third case, a bode diagram of the open-loop system is shown in Fig. 9. As can be seen, there is no -180° crossing in the phase plot regardless of whether or not the resonance frequency is higher than $f_s/4$, which makes the system unstable. Therefore, the system is stable only when the first case is satisfied. Actually, the resonance frequency shifts when the proposed CCFAD is adopted. The effect of the paralleled impedance on the resonance frequency will be discussed in the next part.

1) LCL without Damping: the structure of an LCL without damping is shown in Fig. 10(a). The transfer impedance Z_1 can be expressed as:

$$Z_1 = \dot{U}_{inv} / \dot{I}_2 = j\omega\left(L_1 + L_2 - \omega^2 C L_1 L_2\right) \tag{26}$$

The resonance frequency of the LCL filter without damping can be obtained as (6).

2) LCL with a Resistor Paralleled with a Filter Capacitor: the structure of an LCL with a resistor paralleled with a filter capacitor is shown in Fig. 10(b). The transfer impedance Z_2 can be expressed as:

$$Z_2 = \dot{U}_{inv} / \dot{I}_2 = -\omega^2 L_1 L_2 / R_d + j\omega\left(L_1 + L_2 - \omega^2 C L_1 L_2\right) \tag{27}$$

The resonance frequency of the LCL with a resistor

paralleled with a filter capacitor is the same as (6). Therefore, a resistor paralleled with a filter capacitor does not change the resonance frequency. Comparing (27) with (26), the real part of Z_2 is increased more than Z_1, which means that the system damping is increased.

3) LCL with a Reactor Paralleled with a Filter Capacitor: the structure of an LCL with a reactor paralleled with a filter capacitor is shown in Fig. 10(c). The transfer impedance Z_3 can be expressed as:

$$Z_3 = \dot{U}_{inv} / \dot{I}_2 = j\omega\left(L_1 + L_2 - \omega^2 CL_1L_2 + \omega L_1L_2 / X_d\right) \quad (28)$$

The resonance frequency of the LCL with a reactor paralleled with a filter capacitor can be obtained as (29). Comparing (29) with (6), a reactor paralleled with a filter capacitor changes the resonance frequency. The resonance frequency increases when $X_d > 0$. Similarly, comparing (28) with (26), the imaginary part of Z_3 is higher than Z_1, which means that the system damping is increased.

$$\omega_r = \frac{1}{2CX_d} + \sqrt{\frac{L_1 + L_2}{CL_1L_2} + \left(\frac{1}{2CX_d}\right)^2} \quad (29)$$

4) LCL with a Resistor and a Reactor Paralleled with a Filter Capacitor: the proposed CCFAD method can be seen as a virtual resistor and a reactor paralleled with the filter capacitor shown in Fig. 10(d). The transfer impedance Z_4 can be expressed as:

$$Z_4 = \frac{\dot{U}_{inv}}{\dot{I}_2} = -\frac{\omega^2 L_1L_2}{R_d} + j\omega\left(L_1 + L_2 - \omega^2 CL_1L_2 + \omega\frac{L_1L_2}{X_d}\right) \quad (30)$$

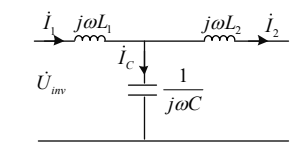

(a)

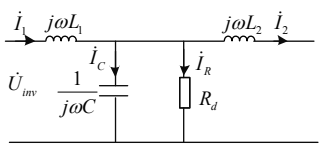

(b)

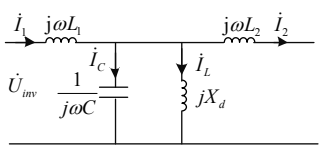

(c)

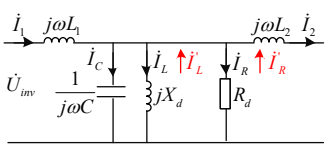

(d)

Fig. 10. Structure of: (a) LCL filter without damping; (b) capacitor paralleled with a resistor; (c) capacitor paralleled with a reactor; (d) capacitor paralleled with both a resistor and a reactor.

The resonance frequency of an LCL with a resistor and a reactor paralleled with a filter capacitor is the same as (29). Comparing (30) and (29) with (26) and (6), the paralleled reactor changes the resonance frequency and when $X_d > 0$, and the resonance frequency shifts to the right. The resistor and reactor can both enhance the damping effect. However, the resistor plays a more important role.

In Fig. 10(d), the defined currents $\dot{I}'_L$ and $\dot{I}'_R$ through the paralleled reactor and resistor are opposite the previous currents, which corresponds to the positive feedback in Fig. 5. Despite the opposite currents, the values of the impedance and resonance frequency remain unchanged as (30) and (29). The equivalent reactor in Fig. 8 acts as an inductor in $(0, f_s/4)$ since the reactance is positive. Thus, the actual resonance frequency decreases. It behaves as a capacitor in $(f_s/4, f_s/2)$ since the reactance is negative. Thus, the actual resonance frequency increases.

E. Performance Evaluation of the CCFAD System with $\lambda = 1$

According to the previous analysis in Section III-C, the proposed CCFAD system with $\lambda = 1$ is stable only in the following two cases, where no unstable open-loop poles exist.

1) $f_r < f_s/4$, $0 < H < H_2$, N = 0.

2) $f_r > f_s/4$, $0 < H < H_3$, N = 0.

Take $f_{r1} < f_s/4$ and $f_{r2} > f_s/4$ for example, where discrete bode diagrams are shown in Fig. 11. The parameters are displayed in Table I, where f_{act1} and f_{act2} are the actual resonance frequencies (f_{act1} = 1.03 kHz, f_{r1} = 1.04 kHz, f_{act2} = 1.43 kHz and f_{r2} = 1.42 kHz). The relationship of $f_{act1} < f_{r1}$ and $f_{act2} > f_{r2}$ validates the previous analysis. The magnitude and phase margin with H and K_p in Table I are 4-10dB and 45-80°, respectively. These values meet the requirements of a stable system.

Fig. 12 shows a closed-loop zero-pole map with the improved CCFAD method, where $f_{r1} < f_s/4$ and $f_{r2} > f_s/4$. As can be seen in this figure, the closed-loop poles tend to move to the center of the unit circle by properly increasing H. This improves the dynamic responses of the system.

TABLE I
PARAMETERS OF THE IMPROVED CCFAD

Parameters	**1)**	**2)**
Inverter-side inductance L_1(mH)	1.5	1.5
Filter capacitor C(μF)	18.8	18.8
Grid-side inductance L_2 (mH)	7.2	1.2
Sampling frequency f_s(kHz)	5	5
Switching frequency f_{sw}(kHz)	5	5

Feedback coefficient H	0.3	0.9
Controller gain K_p	6	6
Resonance frequency f_r(kHz)	1.04	1.42
Magnitude margin K_g(dB)	9.8	4.01
Phase margin γ	76.7°	47.2°

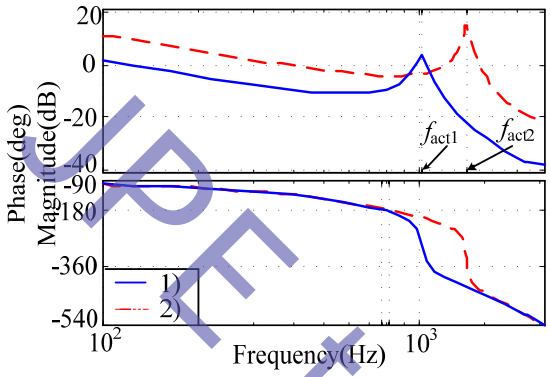

Fig. 11. Bode diagrams of the improved capacitive current proportional feedback system.

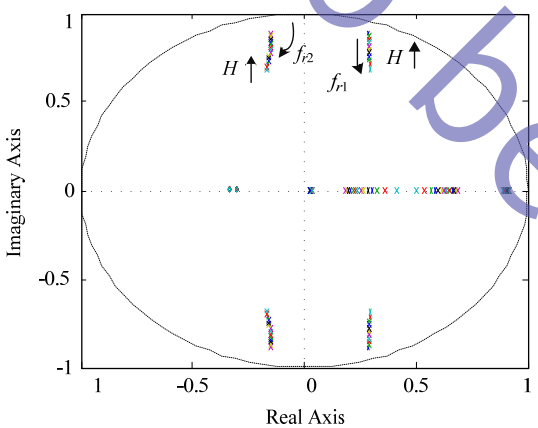

Fig. 12. Closed-loop zero-pole map of the improved CCFAD system.

IV. Simulation and Experimental Results

A simulation model is built in MATLAB/Simulink to verify the validity and feasibility of the proposed CCFAD system. The inverter prototype in this paper uses Infineon's BSM50GB120DLC type IGBTs. The main parameters of the IGBT, which are from its data sheet, are shown in Table II. As can be seen in Table II, the rated output rms current is 50A. To ensure that the loss of IGBT (diode) does not exceed the maximum loss, the appropriate switching frequency range is set to 0.5kHz~11kHz. The switching frequency cannot be lower than 0.5kHz. This is due to the fact that a lower switching frequency leads to increased voltage harmonics. In addition, a higher switching frequency results in a lower maximum output rms current. Therefore, the switching frequency should be lower than 5.5kHz to make sure that the maximum output rms current can be higher than 50A. Finally, in order to obtain better sinusoidal voltage waveforms, this paper selects 5kHz as the switching frequency.

TABLE II
Main Parameters of a BSM50GB120DLC IGBT

Parameter	Value
Collector-emitter voltage U_{CES}	1200V
Output rms current I_{rms}	50A
Operation temperature T_{vj}	125°C
Total power dissipation P_{tot}	460W
Turn on delay time $t_{d(on)}$	0.05μs
Rise time t_r	0.05μs
Turn off delay time $t_{d(off)}$	0.25μs
Fall time t_f	0.03μs

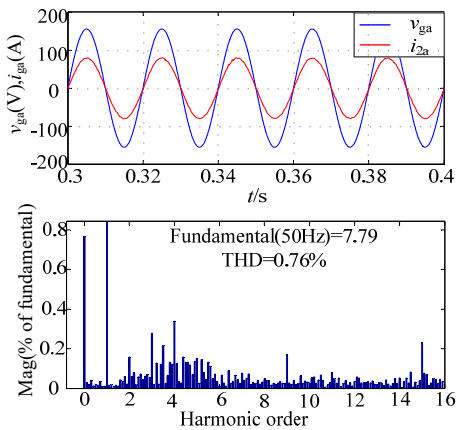

(a)

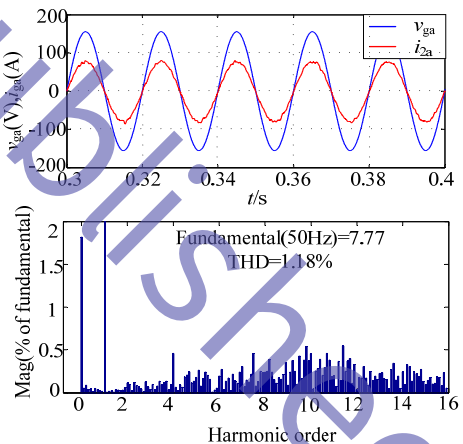

(b)

Fig. 13. Simulation results with different resonance frequencies: (a) $f_r < f_s/4$, f_{r1} = 1.04 kHz; (b) $f_r > f_s/4$, f_{r2} = 1.42 kHz.

Fig. 13 shows waveforms of the voltage, current and total harmonic distortion (THD) of the grid-side current when f_{r1} = 1.04 kHz and f_{r2} = 1.42 kHz.

Fig. 13(a) and Fig. 13(b) are the simulation results obtained when $f_r < f_s/4$ and $f_r > f_s/4$, respectively. The values of H and K_p are consistent with Table I. The current waveform is magnified by 10 times for easier observation in

the diagram of the voltage-current. In Fig. 13(b), the system operates stably when $f_r > f_s/4$, which illustrates that the valid damping region is extended to $(0, f_s/2)$ by the proposed method. The THD is 0.76% when $f_r < f_s/4$ and it is 1.18% when $f_r > f_s/4$. Therefore, the proposed CCFAD provides a satisfactory THD in both of the above occasions.

A 2kW three-phase grid-connected inverter prototype is built to further validate the proposed method with the parameters shown in Table I. A FPGA and DSP together work as the controller of the system.

Fig. 14 shows the dynamic response when the damping method is changed from the proportional CCFAD to the improved CCFAD. It also shows that the system with the improved active damping method can run stably regardless of whether $f_r < f_s/4$ or $f_r > f_s/4$.

Fig. 15 and Fig. 16 show waveforms of voltage and grid-side current in phase-A when $f_r < f_s/4$ and $f_r > f_s/4$, respectively. Fig. 15(a) and Fig. 16(a) indicate the steady-state performance when the reference current is 8A. Fig. 15(b) and Fig. 16(b) indicate the dynamic response when the reference current changes from 8A to 12A. Fig. 15(c) and Fig. 16(c) indicate the resonance performance when K_p changes from 6 to 8.5. Comparing Fig. 15(a) and Fig. 15(c) with Fig. 16(a) and Fig. 16(c), it can be seen that a proper K_p provides a unit-power-factor performance and avoids resonance. Fig. 15(b) and Fig. 16(b) show voltage-current waveforms with the reference current changing from 8A to 12A. It shows that the current tracks the reference signal in 20ms and that the system runs stably with no stable error.

Fig. 17(a) and Fig. 17(b) show the three-phase grid-side current when $f_r < f_s/4$ and $f_r > f_s/4$, respectively. The reference current is 8A and K_p = 6. These results illustrate that the system operates stably in $(0, f_s/4)$ and $(f_s/4, f_s/2)$ with the proposed method.

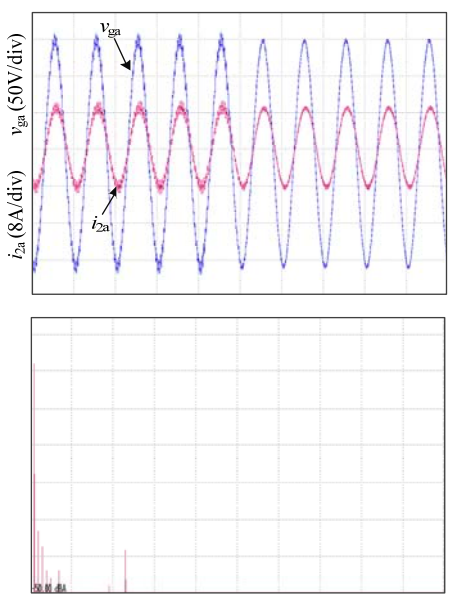

(a)

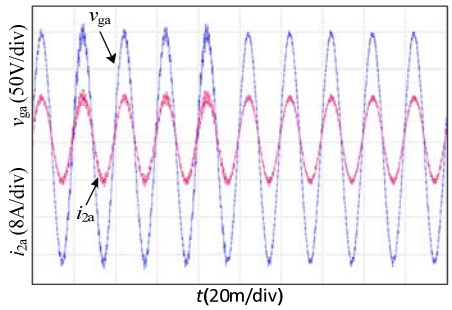

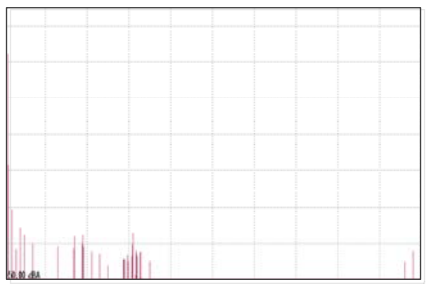

(b)

Fig. 14. Waveforms of the phase-A voltage and current with and without the proposed CCFAD: (a) $f_r < f_s/4$; (b) $f_r > f_s/4$.

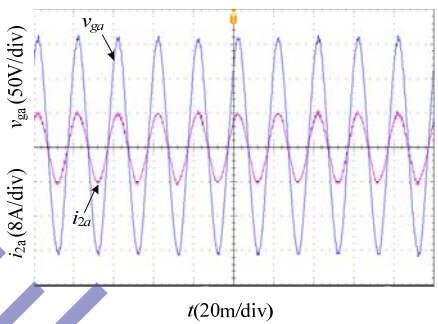

(a)

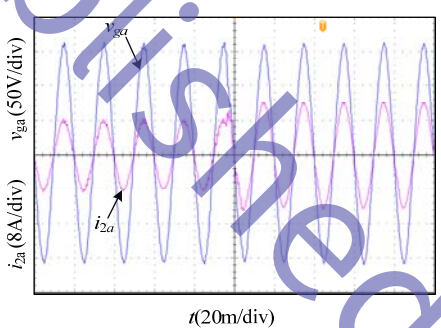

(b)

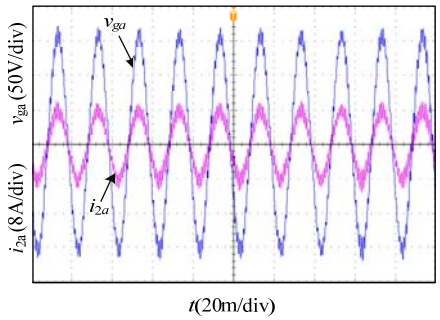

(c)

Fig. 15. Waveforms of the phase-A voltage and current with $f_r < f_s/4$: (a) steady-state; (b) dynamic-state; (c) resonant-state.

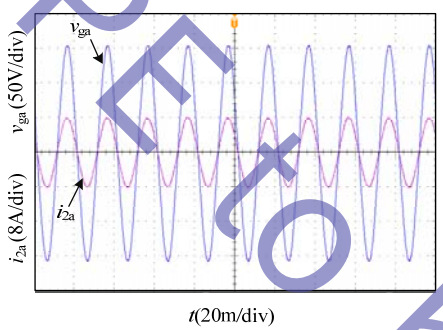

(a)

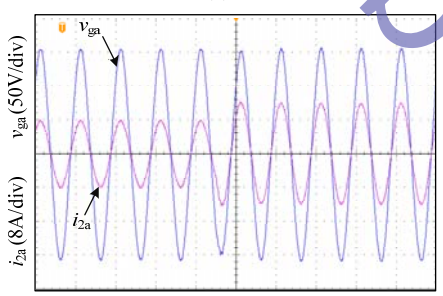

(b)

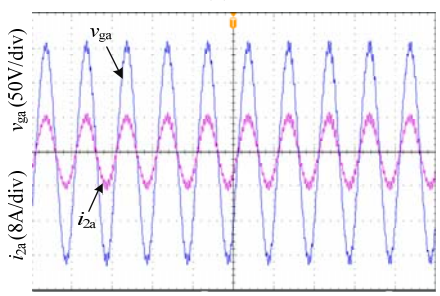

(c)

Fig. 16. Waveforms of the phase-A voltage and current with $f_r > f_s/4$: (a) steady-state; (b) dynamic-state; (c) resonant-state.

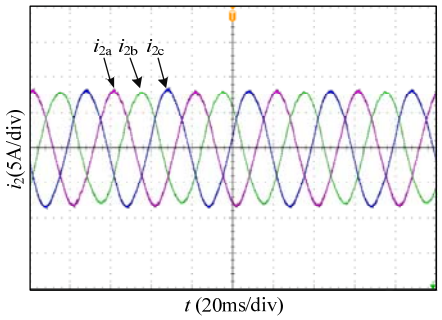

(a)

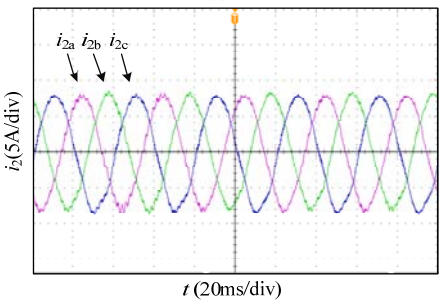

(b)

Fig. 17. Experimental results of the three-phase grid-side current: (a) $f_r < f_s/4$, f_{r1} = 1.04 kHz; (b) $f_r > f_s/4$, f_{r2} = 1.42 kHz.

V. Conclusions

This paper proposes an improved CCFAD method to obtain a full-valid damping region. When compared with the conventional proportional CCFAD, the proposed method extends the valid damping region from (0, $f_s/6$) to (0, $f_s/2$). The feedback link $W(z)$ provides an equivalent virtual impedance to expand the valid damping region. The stability margin is analyzed with a discrete Nyquist criterion. Both simulation and experimental results show that the dynamic performance is improved and that the stability is ensured in the full-valid damping region with a proper feedback coefficient H and controller gain K_p.

References

[1] H. R. Karshenas and H. Saghafi, "Basic criteria in designing LCL filters for grid connected converters," in *2006 IEEE International Symposium on Industrial Electronics*, pp. 1996-2000, 2006.

[2] L. A. Serpa, S. Ponnaluri, P. M. Barbosa, and J. W. Kolar, "A modified direct power control strategy allowing the connection of three-phase inverter to the grid through LCL filters," *IEEE Trans. Ind. Appl.*, Vol. 43, No. 5, pp. 1388-1400, Sept. 2007.

[3] W. Sun, X. Wu, P. Dai, and J. Zhou, "An over view of damping methods for three-phase PWM rectifier," in *2008 IEEE International Conference on Industrial Technology*, pp. 1-5, 2008.

[4] T. C. Y. Wang, Z. Ye, G. Sinha, and X. Yuan, "Output filter design for a grid-interconnected three-phase inverter," in *Proc. 34th IEEE Power Electron. Spec. Conf.*, pp. 779-784, 2003.

[5] W. Yin, and Y. Ma, "Research on three-phase PV grid-connected inverter based on LCL filter," in *Proc. 8th IEEE Conf. Ind. Electron. Appl.*, pp. 1279-1283, 2013.
[6] P. A. Dahono, "A control method to damp oscillation in the input LC filter," in *Proc. 33rd IEEE Power Electron. Spec. Conf.*, pp. 1630-1635, 2002.
[7] J. Xu, S. Xie, and T. Tang, "Active damping-based control for grid-connected *LCL*-filtered inverter with injected grid current feedback only," *IEEE Trans. Ind. Electron.*, Vol. 61, No. 9, pp. 4746-4758, Sep. 2014.
[8] C. Wessels, J. Dannehl, and F. W. Fuchs, "Active damping of LCL-filter resonance based on virtual resistor for PWM rectifiers-stability analysis with different filter parameters," in *Proc. IEEE PESC*, pp. 3532-3538, 2008.
[9] S. G. Parker, B. P. McGrath, and D. G. Holmes, "Regions of active damping control for LCL filters," *IEEE Trans. Ind. Appl.*, Vol. 50, No. 1, pp. 424-432, Jan./Feb. 2014.
[10] M. Wagner, T. Barth, R. Alvarez, C. Ditmanson, and S. Bernet, "Discrete-time active damping of *LCL*-resonance by proportional capacitor current feedback," *IEEE Trans. Ind. Appl.*, Vol. 50, No. 6, pp. 3911-3920, Nov./Dec. 2014.
[11] J. Dannehl, F. W. Fuchs, S. Hansen, and P. B. Thøgersen, "Investigation of active damping approaches for PI-based current control of grid-connected pulse width modulation converters with LCL filters," *IEEE Trans. Ind. Appl.*, Vol. 46, No. 4, pp. 1509-1517, Jul./Aug. 2010.
[12] J. He and Y. Li, "Generalized closed-loop control schemes with embedded virtual impedances for voltage source converters with *LC* or *LCL* filters," *IEEE Trans. Power Electron.*, Vol. 27, No. 4, pp. 1850-1861, Apr. 2012.
[13] C. Bao, X. Ruan, X. Wang, W. Li, D. Pan, and K. Weng, "Step-by-Step controller design for *LCL*-Type grid-connected inverter with capacitor-current-feedback active-damping," *IEEE Trans. Power Electron.*, Vol. 29, No. 3, pp. 1239-1253, Mar. 2014.
[14] D. Pan, X. Ruan, C. Bao, W. Li, X. Wang, "Optimized controller design for *LCL*-type grid-connected inverter to achieve high robustness against grid-impedance variation," *IEEE Trans. Ind. Electron.*, Vol. 62, No. 3, pp. 1537-1547, Mar. 2015.
[15] X. Wang, X. Ruan, C. Bao, D. Pan, and L. Xu, "Design of the PI regulator and feedback coefficient of capacitor current for grid-connected inverter with an *LCL* filter in discrete-time domain," in *Proc. IEEE Energy Conver. Congr. Expo.*, pp. 1657-1662, 2012.
[16] D. Pan, X. Ruan, X. Wang, C. Bao, and W. Li, "Robust capacitor-current-feedback active damping for the *LCL*-type grid-connected inverter," in *Proc. IEEE Energy Conver. Congr. Expo.*, pp. 728-735, 2013.
[17] D. Pan, X. Ruan, C. Bao, W. Li, and X. Wang, "Capacitor-current-feedback active damping with reduced computation delay for improving robustness of *LCL*-type grid-connected inverter," *IEEE Trans. Power Electron.*, Vol. 29, No. 7, pp. 3414-3427, Jul. 2014.
[18] X. Li, X. Wu, Y. Geng, X. Yuan, C. Xia, and X. Zhang, "Wide damping region for *LCL*-type grid-connected inverter with an improved capacitor-current-feedback method," *IEEE Trans. Power Electron.*, Vol. 30, No. 9, pp. 5247-5259, Sep. 2015.
[19] C. Chen, J. Xiong, Z. Wan, J. Lei, and K. Zhang, "A time delay compensation method based on area equivalent for active damping of an *LCL*-type inverter," *IEEE Trans. Power Electron.*, Vol. 32, No. 1, pp. 762-772, Jan. 2017.
[20] Q. Huang and K. Rajashekara, "Virtual RLC active damping for grid-connected inverters with LCL filters," in *Proc. IEEE Applied Power Electronics Conf. Expo.*, pp. 424-429, Mar. 2017.
[21] T. Liu, Z. Liu, J. Liu, Y. Tu, and Z. Liu, "An improved capacitor-current-feedback active damping for the *LCL* resonance in grid-connected inverters," in *Proc. IEEE 3rd International Future Energy Electronics Conf. ECCE Asia.*, pp. 2111-2116, Jun. 2017.
[22] J. L. Agorreta, M. Borrega, J. López, and L. Marroyo, "Modeling and control of *N*-paralleled grid-connected inverters with *LCL* filter coupled due to grid impedance in PV plants," *IEEE Trans. Power Electron.*, Vol. 26, No. 3, pp. 770-785, Mar. 2011.
[23] P. C. Loh, Y. Tang, F. Blaabjerg and P.Wang, "Mixed-frame and stationary-frame repetitive control schemes for compensating typical load and grid harmonics," *IET Power Electron.*, Vol. 4, No. 2, pp. 218-226, Feb. 2011.
[24] R. Peña-Alzola, M. Liserre, F. Blaabjerg, M. Ordonez, and Y. Yang, "LCL-filter design for robust active damping in grid-connected converters," *IEEE Trans. Ind. Informat.*, Vol. 10, No. 4, pp. 2192-2203, Nov. 2014.
[25] C. Bao, X. Ruan, X Wang, W. Li, D. Pan, and K. Weng, "Design of injected grid current regulator and capacitor-current-feedback active- damping for *LCL*-type grid-connected inverter," in *Proc. IEEE Energy Conver. Congr. Expo.*, pp. 579-586. 2012.

Yi-Wen Geng was born in Jiangsu Province, China, in 1977. He received his B.S., M.S. and Ph.D. degrees from the School of Electrical and Power Engineering, China University of Mining and Technology, Xuzhou, China, in 2000, 2004 and 2014, respectively. In 2006, he became a Lecturer in the School of Electrical and Power Engineering, China University of Mining and Technology, where he has been working as an Associate Professor since 2016. His current research interests include photovoltaic inverters, harmonic mitigation, and power electronics.

Ya-Wen Qi was born in Jiangsu Province, China, in 1992. She received her B.S. degree in Electrical Engineering from the China University of Mining and Technology, Xuzhou, China, in 2016, where she is presently working towards her M.S. degree in Electrical Engineering in the School of Electrical and Power Engineering. Her current research interests include the control of converters and harmonic mitigation.

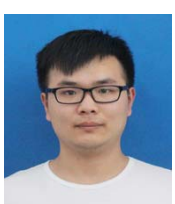

Hai-Wei Liu was born in Jiangsu Province, China, in 1994. He received his B.S. degree in Electrical Engineering from the China University of Mining and Technology, Xuzhou, China, in 2016, where he is presently working towards his M.S. degree in Electrical Engineering in the School of Electrical and Power Engineering. His current research interests include the control of current-source

converters and ac machines.

Fei Guo was born in Anhui Province, China, in 1994. He received his B.S. degree in Electrical Engineering and Automation from the Anhui University, Hefei, China, in 2016. He is presently working towards his M.S. degree in Electrical Engineering in the School of Electrical and Power Engineering, China University of Mining and Technology, Xuzhou, China. His current research interests include the drive systems of permanent magnet synchronous motors for electric vehicles.

Peng-Fei Zheng was born in Anhui Province, China, in 1993. He received his B.S. degree in Electrical Engineering and Automation from the Nanjing University of Posts and Telecommunications, Xuzhou, China, in 2016. He is presently working towards his M.S. degree in Electrical Engineering in the School of Electrical and Power Engineering, China University of Mining and Technology, Xuzhou, China. His current research interests include bidirectional three-level LLC resonant converters and their control.

Yong-Gang Li was born in Henan Province, China, in 1994. He received his B.S. degree in Electrical Engineering from the Shanghai Institute of Technology, Shanghai, China, in 2015. He is presently working towards his M.S. degree in Electrical Engineering in the School of Electrical and Power Engineering, China University of Mining and Technology, Xuzhou, China. His current research interests include the control of multiphase motors and electric vehicles.

Wen-Ming Dong was born in Jiangsu Province, China, in 1992. He received his B.S. degree in Electrical Engineering from the China University of Mining and Technology, Xuzhou, China, in 2015, where he is presently working towards his M.S. degree in Electrical Engineering in the School of Electrical and Power Engineering. His current research interests include the control of inverters and photovoltaic generation technologies.